Chemical Geology 612 (2022) 121144

Contents lists available at ScienceDirect

Chemical Geology

journal homepage: www.elsevier.com/locate/chemgeo

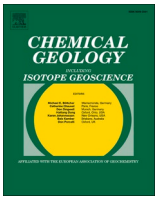

Mercury loss and isotope fractionation during thermal maturation of organic-rich mudrocks

Zeyang Liu [a,b], Hui Tian [a,b,*], Runsheng Yin [c], Di Chen [c], Haifeng Gai [a,b]

[a] State Key Laboratory of Organic Geochemistry, Guangzhou Institute of Geochemistry, Chinese Academy of Sciences, Guangzhou 510640, China
[b] CAS Center for Excellence in Deep Earth Science, Guangzhou, 510640, China
[c] State Key Laboratory of Ore Deposit Geochemistry, Institute of Geochemistry, Chinese Academy of Sciences, Guiyang 550081, China

ARTICLE INFO

Editor: Don Porcelli

Keywords:
Thermal maturity
Mudrock
Volcanism
Kerogen
Source rock correlation
Paleoclimate

ABSTRACT

Mercury (Hg) concentration and isotopic composition of organic-rich sedimentary rocks have been widely used as proxies to track ancient volcanism and associated environmental perturbations. However, interpretation of the Hg data is based on the assumption that the thermal maturity of the sedimentary rocks has limited effects on Hg abundance and isotopic composition, which is yet to be evaluated. Here we conduct closed-system anhydrous pyrolysis experiments to investigate the changes of Hg concentration and isotope composition during the thermal mature process, using both marine and lacustrine mudrocks. A siliceous shale section (Luocun, China) with heterogeneous thermal maturity caused by dike intrusion was also analyzed for Hg. Significant Hg loss (over 80%), with variations of δ^{202}Hg (by 0.3 to 0.7‰) but small variations of Δ^{199}Hg (by <0.1 to 0.36‰), were observed during the experiment. The Hg isotopic variation may be caused by the release of isotopically distinct Hg in different mineral phases at different temperatures. Samples from the Luocun section have anomalously low Hg and Hg/TOC values, due to thermal maturity. These findings suggest that (1) thermal maturation of organic-rich shales may be an important factor in distribution of Hg in sediments, and (2) the use of Hg, Hg/TOC and Hg isotopes proxies for paleoclimate and paleoceanography reconstruction should be applied in caution in substrates that may have experienced significant thermal alteration, especially if sill/dike intrusions were present that may cause large varieties of thermal maturity within sedimentary sections.

1. Introduction

Large igneous provinces (LIPs) played an important role in driving climatic and environmental perturbations in Earth history (e.g., Bond and Grasby, 2017). The large uncertainties associated with radiometric dating of LIPs and sedimentary records hamper direct correlation of volcanic activities with climatic and biotic events. A suite of geochemical toolbox has been used to fingerprint ancient volcanism in the sedimentary records (e.g., osmium [Os] isotope, strontium [Sr] isotope; Du Vivier et al., 2014; Jenkyns, 2010; Liu et al., 2020). Mercury (Hg) anomaly is an abrupt increase in concentrations of Hg and Hg/TOC in the sedimentary archives, which was first introduced by Sanei et al. (2012) as a novel proxy for geological volcanic activities. Application of mercury isotope in the sedimentary records was later discussed by Bergquist (2017) as an additional chemostratigraphic tool for determining heightened volcanism. Mercury anomaly and isotopes have been later used in various studies (e.g., Percival et al., 2015, 2017, 2018, 2020; Grasby et al., 2016, 2019; Shen et al., 2019; Liu et al., 2019a; Jones et al., 2019).

Volcanism via emissions of gaseous and particulate Hg has been the primary natural source of Hg in geological time (Sanei et al., 2012; Grasby et al., 2013; Sanei et al., 2015). In addition, heating of organic-rich sediments by sill intrusions has also been hypothesized to volatilize Hg from the sedimentary rocks (Svensen et al., 2004; Svensen et al., 2009). In large scale volcanism events, the global Hg cycle would be perturbed, leaving a peak of Hg concentration within the sedimentary rocks, to which liberated Hg was then redistributed.

Mercury is strongly bound with organic matter in sedimentary rocks, and thus normalized Hg concentration against total organic carbon content (Hg/TOC) has been used to eliminate the temporal variations of Hg enriched by organic matter (Sanei et al., 2012; Grasby et al., 2013; Sanei et al., 2015). Hg may also be associated with sulfides, and some

* Corresponding author at: State Key Laboratory of Organic Geochemistry, Guangzhou Institute of Geochemistry, Chinese Academy of Sciences, Guangzhou 510640, China.
E-mail address: tianhui@gig.ac.cn (H. Tian).

https://doi.org/10.1016/j.chemgeo.2022.121144
Received 15 February 2022; Received in revised form 10 August 2022; Accepted 21 September 2022
Available online 30 September 2022

clay minerals (e.g., Kongchum et al., 2011; Shen et al., 2020). In addition to Hg enrichment, the isotopic signature of Hg has been used to further identify the two major pathways of volcanic Hg entering the ocean, e.g., atmospheric deposition and terrestrial runoff (Bergquist, 2017; Blum et al., 2014; Grasby et al., 2017; Shen et al., 2019; Sial et al., 2016; Wang et al., 2018; Zheng et al., 2020).

Notably, the current interpretation of Hg data usually ignores the effect of thermal maturity of the sediments on the Hg record. Sedimentary organic matter (kerogen) undergoes thermal degradation in the process of catagenesis (Tissot and Welte, 1984). With the increase of burial depth, kerogen is thermally cracked in response to increasing temperature (typically on a gradient of ~30 °C/km) and produces oil and gas. In the early stages of cracking, kerogen first generates bitumen and oil, and at higher temperatures, the bitumen and oil are further cracked into natural gas. Eventually, up to 60% of the original organic matter might be lost due to secondary migration of the generated products (Lewan et al., 1979; Tissot and Welte, 1984; Raiswell and Berner, 1987). Metals associated with organic matter (e.g., Zn, Cu, Mo, Re and Os) may be transferred into the products of kerogen degradation (Dickson et al., 2020; Selby et al., 2014). Mercury might also transfer into the oil and gas, leading to the enrichment of Hg in oil and natural gas that may pose a significant hazard to the storage and transportation facilities, as well as the environment (Wilhelm, 2001; Tang et al., 2019).

In this study, we conduct closed-system pyrolysis experiments to evaluate the effect of thermal maturation on Hg abundance and isotopic compositions, and to quantify the changes of Hg concentration and isotope during the maturation process of organic-rich mudrocks. Moreover, samples from a section that has been affected by magmatic rock intrusion were also analyzed to evaluate the Hg loss during the thermal alteration process in a geological scenario.

2. Samples

2.1. Samples for pyrolysis experiment

Five low-maturity organic-rich mudrock samples were used in this study, including three marine mudrocks and two lacustrine shales. The marine black shale (XQ1–2) was collected from the Proterozoic Xiamaling Formation (Unit 3) of a core drilled in Zhangjiakou City (Fig. 1, Table 1). This sample has a TOC value of 4.09 wt%, a HI (hydrogen index from Rock–Eval analysis) of 516 mg/g TOC, and contains mainly type IIA kerogen, with Tmax = 439 °C. Sample XJG was collected from the Xiamaling Formation of an outcrop Xiajiagou section next to XQ1–2. This sample has a TOC value of 13.35 wt%, a HI of 476 mg/g TOC, and contains mainly type IIA kerogen, with Tmax = 444 °C. Sample ZLDL is a calcareous mudstone collected from the Talung Formation of the Shangsi section in Guangyuan City. This sample is characterized with a TOC value of 5.56 wt%, a HI of 324 mg/g TOC, and contains mainly type IIB kerogen, with Tmax = 434 °C. The lacustrine back shales (X491 and X491–2) are collected from the fourth member of the Eocene Shahejie Formation (Es4) of a drill core in the Bohai Bay Basin (Fig. 1, Table 1). Sample X491 has a TOC value of 3.45 wt%, a HI of 512 mg/g TOC, and a Tmax value of 426 °C, and its organic matter is dominated by type IIA kerogen. Sample X491–2 has a TOC value of 4.83 wt%, a HI of 281 mg/g TOC, and a Tmax value of 424 °C, and contains type IIB kerogen. (See Fig. 2.)

2.2. Dike intrusion section samples

The Luocun section (N30°C31'46″, E119°C33'41″) is located in Anji County, Zhejiang Province. A 48 m-thick granite dike intruded the Cambrian Hetang Formation consisting of siliceous shales (Fig. 3). The dike has a zircon U—Pb age of 131.8 ± 1.5 Ma and is related to the massive early Cretaceous magmatism in South China (Zhou et al., 2006; Li et al., 2016). This section has been previously investigated with respect to the dike intrusion effect on thermal maturation (Li et al., 2016). It is estimated that the thermal effect of the dike on shale maturation extends a distance of 17.9 m, approximately 37% of the dike width (Li et al., 2016). Twenty-two shale samples were collected in the order of increasing distance to the dike for Hg and TOC analyses (Fig. 3). Three granite samples were also analyzed for their Hg abundance.

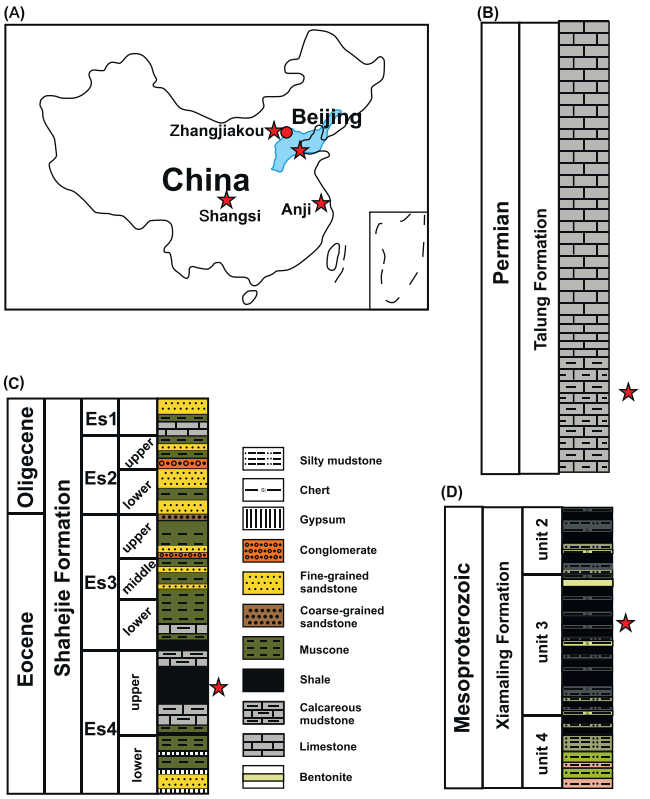

Fig. 1. Schematic maps showing the sampling locations. A: Geographical location of the Bohai Bay Basin and the Zhangjiakou city (Hebei Province) and Anji County (Zhejiang Province); B: Generalized Proterozoic stratigraphy of the northern margin of North China Craton showing the Xiamaling Formation (modified from Zhang et al., 2016); C: Late Permian stratigraphy of the Shangsi section showing the Talung Formation (modified from Liu et al., 2019b); D: Generalized Cenozoic stratigraphy of the Bohai Bay Basin showing the Shahejie Formation (modified from Gai et al., 2018).

Table 1
Geochemical information of samples used for pyrolysis experiments.

Sample ID	S_1[a]	S_2[b]	S_3[c]	Tmax (°C)[d]	HI[e]	OI[f]	TOC (%)
IFP 160000[g]	0.14	12.43	0.79	416	379	24	3.28
IFP 160000	0.19	12.42	0.81	415	380	25	3.27
IFP 160000	0.20	12.21	0.78	416	377	24	3.24
ZLDL	0.76	18.00	0.17	434	324	3	5.56
XQ1–2	1.08	21.09	0.11	439	516	3	4.09
XJG	1.81	63.59	0.53	444	476	4	13.35
X491	0.77	17.66	0.53	426	512	15	3.45
X491–2	0.63	13.59	0.60	424	281	12	4.83

[a] S_1 = free oil content (mg hydrocarbons/g of rock).
[b] S_2 = remaining hydrocarbon potential (mg hydrocarbons/g of rock).
[c] S_3 = organic carbon dioxide (mg CO_2/g of rock).
[d] Tmax = temperature at maximum evolution of S_2 hydrocarbons.
[e] HI = Hydrogen Index (mg hydrocarbon/g TOC).
[f] OI = Oxygen Index (mg CO_2/g TOC).
[g] Certified material value.

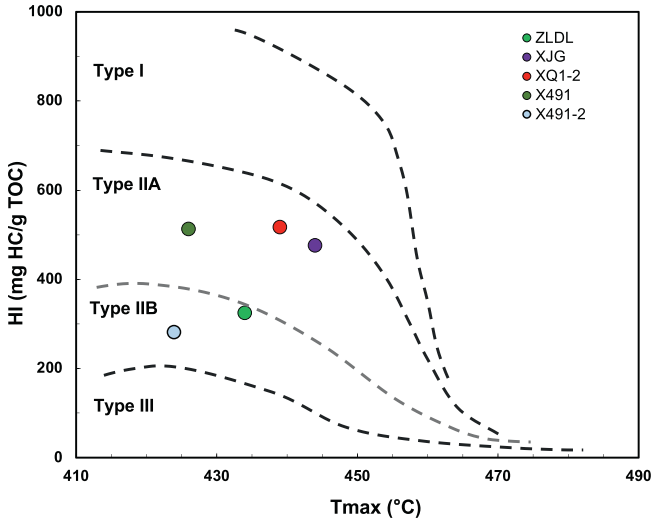

Fig. 2. Hydrogen index-Tmax crossplot for kerogen types, after Mukhopadhyay et al. (1995).

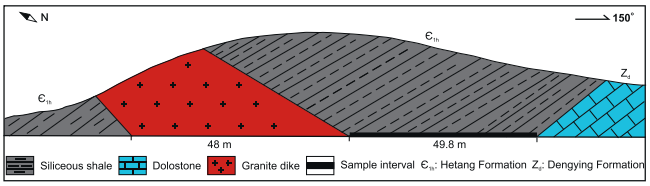

Fig. 3. Sample locations at the Luocun section.

3. Methods

Surface of the samples was removed to obtain fresh samples. The samples were polished on a silicon carbide plate, homogenized and crushed into powders (~200 mesh) using agate mill and puck.

3.1. Pyrolysis experiment

Anhydrous pyrolysis experiments were performed following a previously published procedure (Gai et al., 2018). In brief, ~ 0.8–1.5 g sample powder was loaded into a one-side pre-weld gold tube. The tubes were then put into a box with a constant flow of Ar gas at 20 L/min for 20 mins to remove the O_2. Then, the other side was sealed in argon gas. The gold tubes were then placed into a stainless steel vessel. Pyrolysis experiments were conducted at a confining pressure of 50 MPa. The experimental temperature was first programmed from room temperature to 240 °C in 10 h, and then increased to 610 °C at a heating rate of 20 °C/h. The accuracy of the temperature and pressure measurements were better than 0.5 °C and 1 MPa, respectively. The individual vessel was removed from the oven and immediately cooled by quenching in water once the target temperature was reached. The gold tubes were cut open in a fume hood to allow the gaseous content to escape for about 5 mins, and the samples were then powdered again using agate pestle and mortar.

The temperatures of the pyrolysis experiment were transformed into equivalent vitrinite reflectance (EqVRo) values for geological extrapolation. The temperatures were first converted to Easy%Ro values using the model of Sweeney and Burnham (1990) and the Easy%Ro values were then converted into equivalent vitrinite reflectance (EqVRo) values using the equation from Tang et al. (1996). Calculated EqVRo values range from 0.74% to 3.27%.

3.2. Hg abundance and isotopic composition anlyses

Hg concentration and isotope composition were determined at the State Key Laboratory of Ore Deposit Geochemistry, Institute of Geochemistry, Chinese Academy of Sciences. Total Hg concentrations: Total Hg concentrations were determined using a Lumex RA-915 Hg analyzer. The Lumex RA-915 analyzer was routinely calibrated, and data accuracy and precision were assessed by analyzing procedural blanks, certified standard reference materials (GSS-5, soil) and sample duplicates. Duplicate analysis of Hg concentrations, overall, shows a small relative standard deviation (within ±10%). Total Hg concentrations reported in this study are the average value of the duplicate tests.

Prior to Hg isotope analysis, Hg in the sample powders was preconcentrated into 10 mL of 40% mixed acid solution (*v*/v, HNO_3/HCl = 2:1) using a double-stage combustion method (Sun et al., 2013). The preconcentrated solutions were diluted to 1 ng/mL Hg in 10% acid and were analyzed using an online Hg(0) vapour generation system connected to Neptune Plus multi-collector inductively coupled plasma mass spectrometry (MC-ICP-MS) (Yin et al., 2016). Specifically, Hg(II) in the preconcentrated solutions was continuously reduced by $SnCl_2$ to generate a consistent and pure gaseous Hg(0) flow that was introduced to MC-ICP-MS for Hg isotope measurement (Yin et al., 2016). Isotopic ratios were corrected for mass bias by standard-sample-standard bracketing using NIST-3133 Hg standard solution. Hg isotopic compositions are reported as delta values (δ) in per mil (‰) relative to the mean ratios measured for the NIST-3133 before and after each sample using eq. (1) (Bergquist and Blum, 2007):

$$\delta^{xxx}\mathrm{Hg}\ (‰) = \left[\left(^{xxx}\mathrm{Hg}/^{198}\mathrm{Hg}\right)_{\mathrm{sample}} \Big/ \left(^{xxx}\mathrm{Hg}/^{198}\mathrm{Hg}\right)_{\mathrm{NIST-3133}} - 1\right] \times 1000 \quad (1)$$

where xxx refers to the mass of each Hg isotope between 199 and 204. MIF is reported in capital delta values (Δ), which is the difference between the measured isotopic compositions (δ^{xxx}Hg) and the theoretically predicted values based on the kinetic MDF law (eq. 2):

$$\Delta^{xxx}\mathrm{Hg}\ (‰) = \delta^{xxx}\mathrm{Hg}_{\mathrm{sample}} - \beta \times \delta^{202}\mathrm{Hg}_{\mathrm{sample}} \quad (2)$$

where xxx refers to the mass of Hg isotope. β is 0.252, 0.502, 0.752 for Δ^{199}Hg, Δ^{200}Hg and Δ^{201}Hg, respectively. Analytical uncertainty was estimated based on the replicates of the NIST 8610 secondary standard solution and full procedural analyses of soil standard reference material GSS-4. The overall average and uncertainty of NIST-8610 (δ^{202}Hg: −0.54 ± 0.11‰; Δ^{199}Hg: −0.03 ± 0.07‰; Δ^{200}Hg: 0.01 ± 0.05‰; Δ^{201}Hg: −0.01 ± 0.06‰; 2SD, n = 6) and GSS-4 (δ^{202}Hg: −1.73 ± 0.12‰; Δ^{199}Hg: −0.36 ± 0.08‰; Δ^{200}Hg: −0.02 ± 0.05‰; Δ^{201}Hg: −0.35 ± 0.06‰; 2SD, n = 3) agree well previous results (Bergquist and Blum, 2007; Deng et al., 2020). Uncertainties reported in this study correspond to the larger value of either (1) the measurement uncertainty of replicate digests of GSS-4, or (2) the uncertainty of repeated measurements of NIST-8610.

3.3. Total organic carbon and Rock-Eval analysis

An aliquot of the sample powder was treated with 2 M HCl to remove the carbonates and then dried at ~60 °C. Total organic carbon contents were then determined with a Leco C/S analyzer using the direct combustion method. Mudrock standards with a certified TOC value of 1.86% were used for quality control. Programmed pyrolysis was performed on a Rock-Eval 6 instrument. Rock-Eval standard of IFP 160000 was used for quality control.

3.4. X-ray diffraction analysis

The mineral composition of the samples (including those pyrolysed samples with enough material to make a pellet) was analyzed by Rigaku

MiniFlex-600 X-ray diffraction (XRD) analytical measuring instrument, which was equipped with a Ni filter and Cu Kα radiation (40 kV and 15 mA). The diffraction patterns were collected from 3° to 80° 2θ at a scanning rate of 10°/min.

4. Results

During the pyrolysis experiment, significant Hg loss was observed for all the samples, with a similar evolutionary profile for Hg loss showing the majority of Hg (over 80%) was lost when heated at 485 °C (Fig. 4A). The Hg/TOC values for the samples share a similar profile with Hg abundance due to the relatively large variation of Hg concentration compared with limited TOC change (e.g., over 80% loss for Hg vs. <30% loss for TOC, Fig. 4B).

Hg isotope variation in the samples, with increasing temperature, is shown in Fig. 5. A positive increase of 0.3‰ in δ^{202}Hg values but no variation of Δ^{199}Hg (<0.1‰), are observed for the lacustrine sample X491. Similarly, lacustrine sample X491–2 shows a small increase of 0.29‰ in δ^{202}Hg and minor variations in Δ^{199}Hg (0.12‰) within the heating process. A negative shift of δ^{202}Hg (by 0.39‰) is observed in marine mudrock sample XQ1–2, but Δ^{199}Hg only shift by 0.07‰. Sample XJG has limited isotopic variation under most heating temperatures, but both δ^{202}Hg and Δ^{199}Hg shift to lower values (by 0.39‰ in δ^{202}Hg and by 0.36‰ in Δ^{199}Hg) at 460 °C, and represents the largest Δ^{199}Hg variation among samples. Sample ZLDL shows large variation of δ^{202}Hg (by 0.69‰) and Δ^{199}Hg (by 0.28‰), with an overall increase pattern for both δ^{202}Hg and Δ^{199}Hg values over the heating process.

5. Discussion

5.1. Hg concentration and isotope change during the thermal mature process

Both the marine and lacustrine mudrocks experienced dramatic Hg loss (over 80%) in the pyrolysis experiment (Fig. 4). The pyrolysis

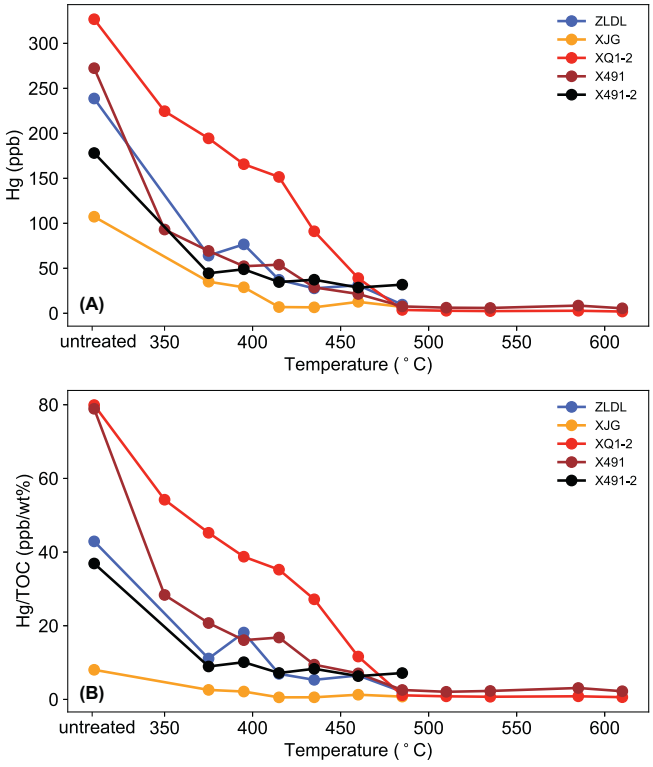

Fig. 4. Evolution of Hg and Hg/TOC with pyrolysis temperature.

experiment is involved with kinetic reactions of cracking kerogen bonds and forming hydrocarbon chains, and it is known that kinetic reactions result in lighter δ^{202}Hg values for products and heavier δ^{202}Hg values for the residues (Blum et al., 2014). The trend to heavier δ^{202}Hg values of the two lacustrine shales (Fig. 5) is consistent with the theoretic prediction for Hg-MDF during kinetic processes, during which lighter Hg isotopes are preferentially lost. The other three marine shales show either a trend to lighter δ^{202}Hg values or fluctuation of δ^{202}Hg values with no clear trend (Fig. 5), may be explained by (1) inhomogeneous Hg isotopic composition in the sample powder or (2) release of Hg from different mineral phases (associated with different δ^{202}Hg values) in different heating stages. Overall, the variation of δ^{202}Hg (0.3 to 0.7‰) the pyrolysis experiment is similar to that observed during the liberation of Hg from sedimentary rocks by hydrothermal fluids (80–150 °C) (within 0.5‰; Smith et al., 2008). In contrast, volatilization of Hg(0) from aqueous solution at room temperature results in larger fractionation of δ^{202}Hg (up to 1.5‰; Zheng et al., 2007). Fluids (liquid hydrocarbons) may be an important conduit for Hg. The fluid composition may have serious impacts on bulk isotopes, and may potentially explain the noise in δ^{202}Hg, which appears at intermediate heating temperatures where fluid liberation in the experimental samples will be peaking. Hg could have transferred from kerogen into liquid hydrocarbons, and then transferred into the gas phase with the hydrocarbon cracking process. However, as the majority of Hg (over 80%) was lost with the gas, the Hg remained in the liquid phase of the residues is limited, and should not account for the overall Hg isotope variations observed in this study (Fig. 5).

Hg-MIF signals in natural samples are mainly triggered by photochemical reduction on Earth's surface (Blum et al., 2014). Given the lack of photoreactions during the pyrolysis experiment, it is expected that Δ^{199}Hg would not be changed during the experiment. This is supported by the minor Δ^{199}Hg variations in the studied samples, i.e., most data points show Δ^{199}Hg variation of 0.10‰, given the analytical error of ±0.08‰ for Δ^{199}Hg (Fig. 5).

A few data points for two mudrocks (XJG-435 and ZLDL-460) show large variations in Δ^{199}Hg (by 0.28 to 0.36‰). While sample heterogeneity can cause the observed Δ^{199}Hg variations, this seems unlikely due to the samples being carefully powdered and homogenized. An alternative explanation is that Hg is hosted by different phases with distinct Δ^{199}Hg. Mercury is hosted in multiple fractions such as organic matter, sulphides, and clay minerals (e.g., Shen et al., 2020; Them et al., 2019), which may carry different Hg isotope signals. It has been shown that the epigenetic pyrite fractions have higher Δ^{199}Hg values than the organic fractions in coal (Lefticariu et al., 2011). Mercury in different fractions of sediments can be released at different temperatures during thermal pyrolysis (Guo et al., 2012; Luo et al., 2011; Sun et al., 2013), which may cause Hg isotopic variation in the thermal-altered samples. With the heating progress, the lacustrine samples X491 and X491–2 show increasing amounts of illite and reducing amounts of kaolinite, with the gypsum changing to anhydrite, while the clay mineral and pyrite contents remain relatively constant (Table 3). The marine sample XQ1–2 has a relatively constant mineral composition during the heating progress. Since clay mineral has the least affinity of Hg compared with organic matter and pyrite, it is difficult to attribute the Hg isotope variations to the changes of the clay mineral compositions. Overall, we suggest that the release of different Hg phases associated with distinct Hg isotopic signals at different temperatures may be the reason for the variations of δ^{202}Hg and Δ^{199}Hg in our samples.

5.2. Hg and Hg/TOC signature of the dike intruded Luocun section

The studied region is suggested to have experienced steady marine deposition since the early Cambrian to middle Triassic, and terrestrial deposition from the late Triassic to early Cretaceous (Guo, 1996). The Hetang Formation experienced multiple tectonic movement and Cretaceous granite intrusion and Cenozoic volcanism. The maximum burial

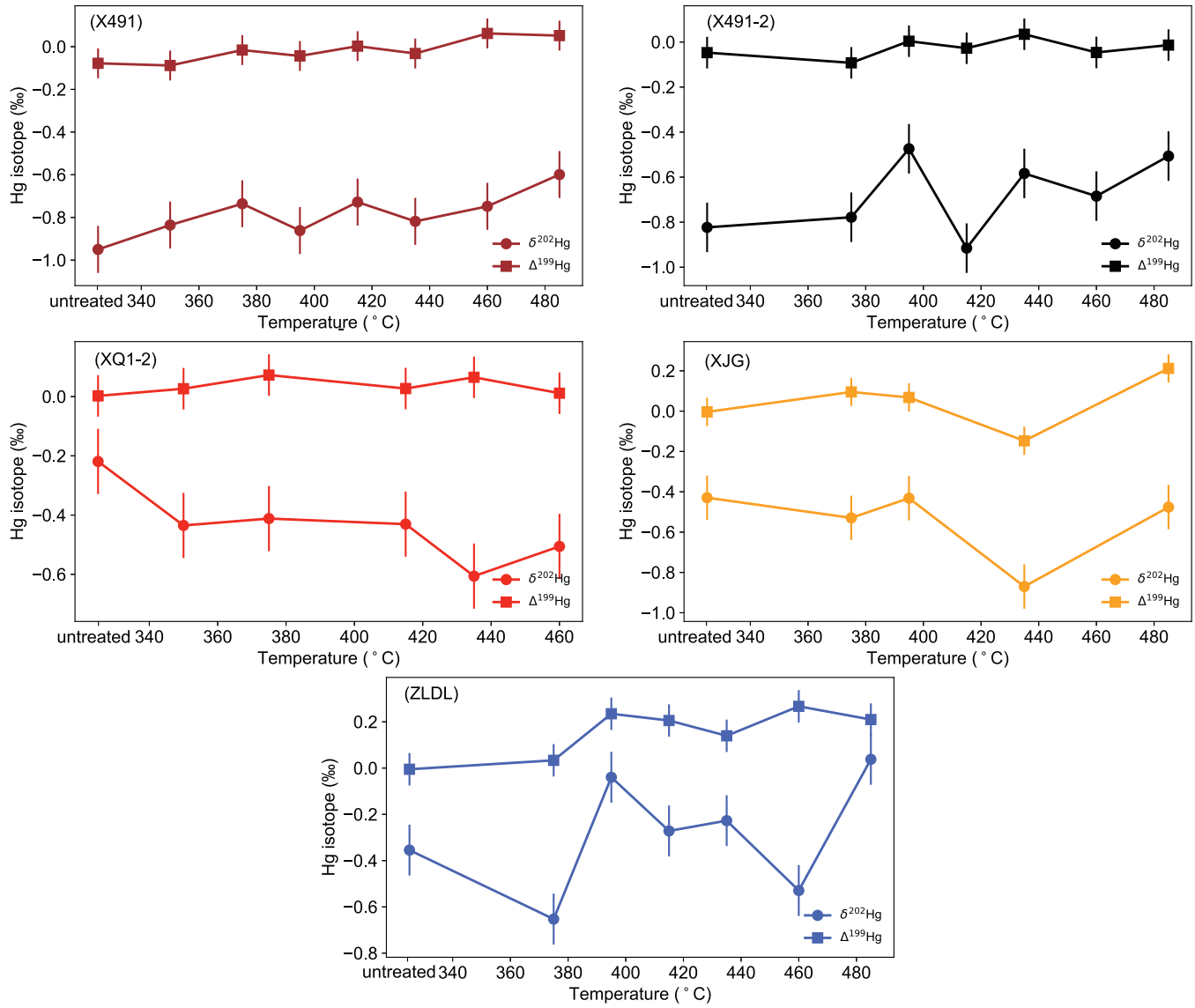

Fig. 5. Evolution of Hg isotope compositions with pyrolysis temperature.

depth is estimated to be up to 4500 m, with BRo values generally over 2%, and higher BRo values over 4% in the areas where volcanic rocks are present (Wang et al., 2016). Based on the BRo values of the Luocun section, we summarise that the section experienced a burial history that heated the section to 3.1% (BRo, Li et al., 2016), and the dike intrusion further heated the section up to 5.4% (BRo, Fig. 6). In contrast to the pyrolysis experiment, the Hg abundance and Hg/TOC values of the geological samples do not show a correlation with thermal maturity values (BRo, Fig. 6). Unlike the clear trend of increasing BRo values towards the dike, the Hg and Hg/TOC values are varying at a small range (0.21 to 2.02 ppb and 0.19 to 3.29 ppb/wt%, respectively). We need to note that the samples are not perpendicular to the dike, as thus the variations are linked with the stratigraphic variations. However, it is noteworthy that the Hg and Hg/TOC values are significantly lower than the postulated average shale concentrations (62.4 ppb Hg and 71.9 ppb/wt% Hg/TOC, Grasby et al., 2019). Though the original Hg abundance is hard to know, using the average shale value of 62.4 ppb, the average measured Hg concentration values of the Hetang Formation (0.89 ppb, $n = 22$) are in consistent with the laboratory simulation that over 80–99% of Hg was lost during the thermal maturation process. The anomalously low Hg concentration of the Hetang Formation is best interpreted by the thermal maturation along with the burial history. Further Hg loss could have been caused by the heating from dike intrusion, and/or the magmatic rocks underlying the section, however, its effect is probably limited, as the majority of Hg has already been lost during the burial thermal maturation. Another aspect worthy to be mentioned is that the magma might release fluids that diffuse into the country rock during the intrusion process (Li et al., 2016). However, little Hg could have been transferred from the granitic magma into the country rock through this process, as the granite samples have very low Hg abundances (0.12 to 0.27 ppb, Table 2).

5.3. *Implications for using Hg as a proxy for paleoclimate and paleoceanography*

Both the Hg concentration and isotope composition are used for paleoclimatic and paleoceanographic research (e.g., Grasby et al., 2017; Grasby et al., 2019; Sanei et al., 2012; Sial et al., 2016; Wang et al., 2018). A rise in the Hg concentration and Hg/TOC values has been used to identify potential intervals of enhanced volcanism. In addition to using Hg concentration variations for identifying large volcanism, δ^{202}Hg and Δ^{199}Hg values of sediments are also used for the

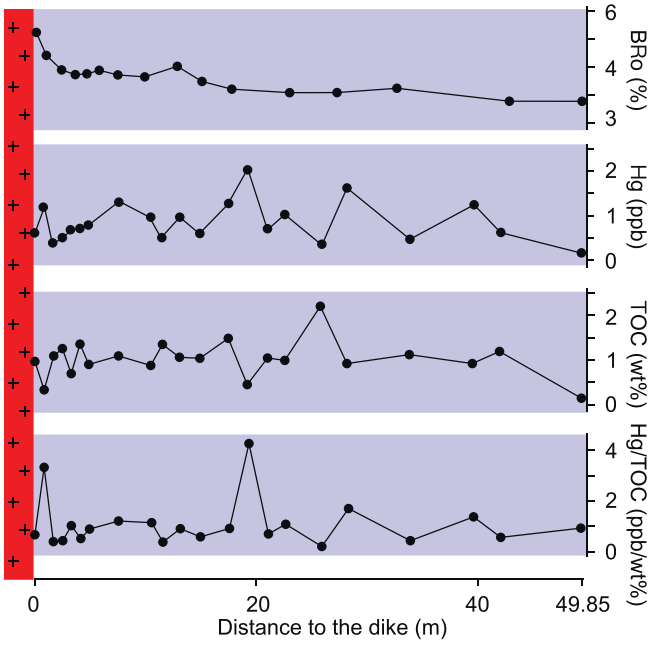

Fig. 6. Hg, TOC and Hg/TOC values of the Luocun section samples. The EqVRo values are from Li et al. (2016).

Table 2
Hg, TOC and Hg/TOC results for Luocun samples.

Sample ID	Distance (m)	Hg (ppb)	TOC (wt %)	Hg/TOC	Lithology
IVA33802153 (TOC = 1.86 wt %)			1.78		
IVA33802153 (TOC = 1.86 wt %)			1.86		
GR-01		0.26			granite
GR-02		0.27			granite
GR-03		0.12			granite
LZY-001	0.00	0.66	0.99	0.66	shale
LZY-002	0.82	1.23	0.37	3.29	shale
LZY-003	1.63	0.41	1.12	0.36	shale
LZY-004	2.45	0.55	1.29	0.42	shale
LZY-005	3.27	0.72	0.71	1.01	shale
LZY-006	4.09	0.74	1.40	0.53	shale
LZY-007	4.90	0.83	0.94	0.89	shale
LZY-008	7.60	1.34	1.10	1.21	shale
LZY-009	10.62	1.00	0.88	1.13	shale
LZY-010	11.60	0.52	1.38	0.38	shale
LZY-011	13.24	0.97	1.09	0.89	shale
LZY-012	15.12	0.62	1.09	0.57	shale
LZY-013	17.73	1.33	1.52	0.87	shale
LZY-014	19.45	2.02	0.48	4.25	shale
LZY-015	21.25	0.74	1.09	0.69	shale
LZY-016	22.88	1.08	1.01	1.07	shale
LZY-017	26.15	0.42	2.22	0.19	shale
LZY-018	28.60	1.64	0.95	1.72	shale
LZY-019	34.32	0.49	1.14	0.43	shale
LZY-020	40.04	1.28	0.95	1.35	shale
LZY-021	42.50	0.67	1.21	0.55	shale
LZY-022	49.85	0.21	0.23	0.95	shale

identification of possible pathways of Hg into the ocean (e.g., terrestrial runoff, atmospheric deposition; Grasby et al., 2019). In contrast, the large changes of Hg concentration, and the variations of δ^{202}Hg values during the thermal maturation process raise questions regarding the interpretation of Hg data (Figs. 4 and 5). However, Hg isotope stratigraphy across intervals that record geologic events (e.g., volcanic activity; Grasby et al., 2017) generally have δ^{202}Hg shift over 2–3‰, which are much larger than the largest shift of δ^{202}Hg observed here (~0.69‰). Thus, we suggest that δ^{202}Hg may still be a useful proxy, but must be cautious when explaining stratigraphic δ^{202}Hg shifts for samples that experienced thermal maturation. By analogy, the stratigraphic shifts of Δ^{199}Hg should also be carefully assessed when using it as a proxy to track the Hg sources, given that different host fractions with distinct Δ^{199}Hg values might be released at different temperatures.

Great caution needs to be taken when there is sill/dike intrusion in the sections investigated that may have large thermal maturity variations within a distance of meters (Li et al., 2016). The studied Luocun section has experienced enormous Hg loss, and the Hg concentration and isotope variations might be caused by maturity rather than their original depositional signature. The significant Hg loss (>80% of the original Hg) during the pyrolysis experiment (Fig. 4) and the anomalously low Hg and Hg/TOC values for the Luocun section (Fig. 6) further support the hypothesis that sill/dike intrusion into organic-rich sediments provides a major source of toxic Hg to the ocean and atmosphere that can disturb the global Hg cycle and Earth environments (Burgess et al., 2017; Grasby et al., 2019).

Similar to any other pyrolysis experiments, the difference between laboratory and geological scenarios needs to be considered. The natural maturation of organic matter in mudrocks is a process of increasing temperature at a much slower speed over a much longer time duration that can never be reconstructed in the laboratory. Moreover, the geological mudrocks are much tighter than the powder samples used in the pyrolysis experiment. As a result, less Hg loss would be expected for the geological samples at other similar conditions. This is probably the reason that some overmature geological shale samples still have Hg concentrations at hundreds of ppb or even ppm levels (Fan et al., 2021). Or, it could be possible that the original Hg concentrations could be much higher than the current measured Hg values (10 to 100 times based on the laboratory experiments). The samples with high thermal maturity may not preserve their original Hg concentration and isotope values at their deposition time (Figs. 4 and 5). For sedimentary successions with thickness of tens to hundreds of meters, the thermal maturity level is not expected to change dramatically when there are no sill/dike intrusions. If the samples experienced a similar degree of Hg loss and isotope change, the geochemistry of Hg might still be insightful for paleoclimate and oceanography reconstructions. Evaluation of the geological backgrounds of investigated sections and samples is, therefore, very important for accurate interpretation of the Hg data.

5.4. Implications for oil and gas fingerprinting

Correlation of oil and gas to their source rocks are vital to oil and gas exploration. Organic geochemical proxies (biomarkers) are commonly used for such correlation because of their wide occurrence in both source rocks and oil and gas (Peters et al., 2005). Hg isotopic compositions might be potentially used as a novel correlation tool that is independent of the organic geochemical proxies (Tang et al., 2019). The small Δ^{199}Hg variation within the progressive pyrolysis process suggests that it can be used as a potential tool to trace the candidate source rocks associated with distinct Hg-MIF signatures. In contrast, the large variation of δ^{202}Hg without clear trends during thermal maturation processes makes it an unreliable proxy to aid the oil/gas-source rock correlation.

6. Conclusions

This study provides evidence of significant Hg loss, decreasing Hg/TOC ratios, and changes in δ^{202}Hg and Δ^{199}Hg during thermal maturation of organic-rich mudrocks, which challenge the potential use of these geochemical proxies for paleoclimate and paleoceanography reconstruction, when dealing with certain types of sedimentary rocks (e.g., high metamorphized rocks or rocks affected by nearby sill/dike intrusions). This study also indicates thermal maturation may be an

Table 3
XRD analysis results. Note that numbers are weight percent of the minerals.

Sample ID	quartz	K feldspar	plagioclase	illite	kaolinite	gypsum	anhydrite	chlorite	pyrite	calcite
ZLDL	74.8	0.9	0	0	0	0	0	0	2.5	21.8
ZLDL-395	73.3	0	0	0	0	4.2	0	0	1.6	20.9
X491–2	8	1.8	5.8	43.9	36.2	1.4	0	0	3	0
X491–2-375	9.2	2.3	4.6	45.5	32.6	0	2.8	0	3	0
X491–2-395	8.6	2.7	4.3	50	29.1	0	2.6	0	2.7	0
X491–2-435	10.2	0	3	55.9	24.3	0	2.8	0	3.8	0
X491	9.4	2.8	6.2	37.3	41.6	0.3	0	0	2.3	0
X491–350	9.8	7.7	5.2	40.4	31.2	0	3.5	0	2.3	0
X491–375	11.4	2.9	7.4	43.3	28.7	0	3.9	0	2.4	0
X491–395	13.2	2.9	8.6	37.8	31	0	3.7	0	2.7	0
X491–415	10	4.9	5.8	42.7	29.6	0	4.6	0	2.3	0
X491–435	13.8	1.6	5.3	50	24.4	0	2.6	0	2.3	0
X491–460	14.7	0	7.8	55.3	17.2	0	2.6	0	2.4	0
XQ1–2	38.8	3.1	1.1	38.6	0	0	0	16.4	2	0
XQ1–2-350	45.7	3	1.9	33.1	0	0	0	14	2.5	0
XQ1–2-375	36.5	2.2	0.9	44.2	0	0	0	14.6	1.5	0
XQ1–2-415	44.2	3.4	0.4	34.8	0	0	0	15	2.2	0
XQ1–2-435	34.6	1.1	1.8	48.5	0	0	0	13	1	0
XQ1–2-460	41.8	2.9	1.3	37.1	0	0	0	16.2	0.7	0
XJG	54.2	2.5	1	30.2	0	3.9	0	8.1	0	0

important driving force to mobilize Hg from geological pools to the environment, which might also depend on the kerogen type and burial depth, and is worthy of further investigation to evaluate its environmental risk as well.

Data availability

Datasets related to this article can be found at https://data.mendeley.com (doi: 10.17632/959r6z2jp9.1), an open-source online data repository hosted at Mendeley Data.

Declaration of Competing Interest

The authors declare no conflict of interest. This manuscript has not been submitted and will not be submitted to any other journals while it is under review for *Chemical Geology*.

Data availability

Data available as supplementary material

Acknowledgements

We thank Qizhang Fan for assistance with laboratory analyses and Wei Liu for field work. We gratefully acknowledge the Natural Science Foundation of China (NSFC Grant No. 41925014) to H.T., NSFC (42173031) to H.G., and the China Postdoctoral Science Foundation (20M682934) and Director's Fund of Guangzhou Institute of Geochemistry, CAS (2020000155) to Z.L. This is contribution No.IS-3252 from GIGCAS.

Appendix A. Supplementary data

Supplementary data to this article can be found online at https://doi.org/10.1016/j.chemgeo.2022.121144.

References

Bergquist, B.A., 2017. Mercury, volcanism, and mass extinctions. Proc. Natl. Acad. Sci. 114, 8675–8677.
Bergquist, B.A., Blum, J.D., 2007. Mass-Dependent and -Independent Fractionation of Hg Isotopes by Photoreduction in Aquatic Systems. Science 318, 417–420.
Blum, J.D., Sherman, L.S., Johnson, M.W., 2014. Mercury Isotopes in Earth and Environmental Sciences. Annu. Rev. Earth Planet. Sci. 42, 249–269.
Bond, D.P.G., Grasby, S.E., 2017. On the causes of mass extinctions. Palaeogeogr. Palaeoclimatol. Palaeoecol. 478, 3–29.
Burgess, S.D., Muirhead, J.D., Bowring, S.A., 2017. Initial pulse of Siberian Traps sills as the trigger of the end-Permian mass extinction. Nat. Commun. 8, 164.
Deng, C., Sun, G., Rong, Y., Sun, R., Sun, D., Lehmann, B., Yin, R., 2020. Recycling of mercury from the atmosphere-ocean system into volcanic-arc–associated epithermal gold systems. Geology 49, 309–313.
Dickson, A.J., Idiz, E., Porcelli, D., van den Boorn, S.H.J.M., 2020. The influence of thermal maturity on the stable isotope compositions and concentrations of molybdenum, zinc and cadmium in organic-rich marine mudrocks. Geochim. Cosmochim. Acta 287, 205–220.
Du Vivier, A.D.C., Selby, D., Sageman, B.B., Jarvis, I., Gröcke, D.R., Voigt, S., 2014. Marine $^{187}Os/^{188}Os$ isotope stratigraphy reveals the interaction of volcanism and ocean circulation during Oceanic Anoxic Event 2. Earth Planet. Sci. Lett. 389, 23–33.
Fan, H., Fu, X., Ward, J.F., Yin, R., Wen, H., Feng, X., 2021. Mercury isotopes track the cause of carbon perturbations in the Ediacaran Ocean. Geology 49, 248–252.
Gai, H., Tian, H., Xiao, X., 2018. Late gas generation potential for different types of shale source rocks: Implications from pyrolysis experiments. Int. J. Coal Geol. 193, 16–29.
Grasby, S.E., Sanei, H., Beauchamp, B., Chen, Z., 2013. Mercury deposition through the Permo–Triassic Biotic Crisis. Chem. Geol. 351, 209–216.
Grasby, S.E., Beauchamp, B., Bond, D.P.G., Wignall, P.B., Sanei, H., 2016. Mercury anomalies associated with three extinction events (Capitanian Crisis, latest Permian Extinction and the Smithian/Spathian Extinction) in NW Pangea. Geol. Mag. 153, 285–297.
Grasby, S.E., Shen, W., Yin, R., Gleason, J.D., Blum, J.D., Lepak, R.F., Hurley, J.P., Beauchamp, B., 2017. Isotopic signatures of mercury contamination in latest Permian oceans. Geology 45, 55–58.
Grasby, S.E., Them, T.R., Chen, Z., Yin, R., Ardakani, O.H., 2019. Mercury as a proxy for volcanic emissions in the geologic record. Earth Sci. Rev. 196, 102880.
Guo, N.F., 1996. The Yangtze basin and the regional tectonic evolution characteristics and the analysis of hydrocarbon accumulation. Geol. Zhejiang 12, 19–27 (in Chinese).
Guo, S., Yang, J., Liu, Z., 2012. Characterization of Hg in coals by temperature-programmed decomposition–atomic fluorescence spectroscopy and acid-leaching techniques. Energy Fuel 26, 3388–3392.
Jenkyns, H.C., 2010. Geochemistry of oceanic anoxic events. Geochem. Geophys. Geosyst. 11.
Jones, M.T., Percival, L.M.E., Stokke, E.W., Frieling, J., Mather, T.A., Riber, L., Schubert, B.A., Schultz, B., Tegner, C., Planke, S., Svensen, H.H., 2019. Mercury anomalies across the Palaeocene–Eocene Thermal Maximum. Clim. Past 15, 217–236.
Kongchum, M., Hudnall, W.H., Delaune, R.D., 2011. Relationship between sediment clay minerals and total mercury. J. Environ. Sci. Health A 46, 534–539.
Lefticariu, L., Blum, J.D., Gleason, J.D., 2011. Mercury Isotopic evidence for Multiple Mercury sources in coal from the Illinois Basin. Environ. Sci. Technol. 45, 1724–1729.
Lewan, M., Winters, J., McDonald, J., 1979. Generation of oil-like pyrolyzates from organic-rich shales. Science 203, 897–899.
Li, X., Wang, Q., Zhang, W., Yin, H., 2016. Contact metamorphism of shales intruded by a granite dike: Implications for shale gas preservation. Int. J. Coal Geol. 159, 96–106.

Liu, Z., Horton, D.E., Tabor, C., Sageman, B.B., Percival, L.M.E., Gill, B.C., Selby, D., 2019a. Assessing the Contributions of Comet Impact and Volcanism toward the climate Perturbations of the Paleocene-Eocene thermal Maximum. Geophys. Res. Lett. 46, 14798–14806.
Liu, Z., Selby, D., Zhang, H., Zheng, Q., Shen, S., Sageman, B.B., Grasby, S.E., Beauchamp, B., 2019b. Osmium-isotope evidence for volcanism across the Wuchiapingian–Changhsingian boundary interval. Chem. Geol. 529, 119313.
Liu, Z., Selby, D., Zhang, H., Shen, S., 2020. Evidence for volcanism and weathering during the Permian-Triassic mass extinction from Meishan (South China) osmium isotope record. Palaeogeogr. Palaeoclimatol. Palaeoecol. 553, 109790.
Luo, G., Yao, H., Xu, M., Gupta, R., Xu, Z., 2011. Identifying modes of occurrence of mercury in coal by temperature programmed pyrolysis. Proc. Combust. Inst. 33, 2763–2769.
Mukhopadhyay, P.K., Wade, J.A., Kruge, M.A., 1995. Organic facies and maturation of Jurassic/cretaceous rocks, and possible oil-source rock correlation based on pyrolysis of asphaltenes, Scotian Basin, Canada. Org. Geochem. 22, 85–104.
Percival, L.M.E., Witt, M.L.I., Mather, T.A., Hermoso, M., Jenkyns, H.C., Hesselbo, S.P., Al-Suwaidi, A.H., Storm, M.S., Xu, W., Ruhl, M., 2015. Globally enhanced mercury deposition during the end-Pliensbachian extinction and Toarcian OAE: A link to the Karoo–Ferrar Large Igneous Province. Earth Planet. Sci. Lett. 428, 267–280.
Percival, L.M.E., Ruhl, M., Hesselbo, S.P., Jenkyns, H.C., Mather, T.A., Whiteside, J.H., 2017. Mercury evidence for pulsed volcanism during the end-Triassic mass extinction. Proc. Natl. Acad. Sci. 114, 7929–7934.
Percival, L.M.E., Jenkyns, H.C., Mather, T.A., Dickson, A.J., Batenburg, S.J., Ruhl, M., Hesselbo, S.P., Barclay, R., Jarvis, I., Robinson, S.A., Woelders, L., 2018. Does large igneous province volcanism always perturb the mercury cycle? Comparing the records of Oceanic Anoxic event 2 and the end-cretaceous to other Mesozoic events. Am. J. Sci. 318, 799–860.
Percival, L.M.E., van Helmond, N.A.G.M., Selby, D., Goderis, S., Claeys, P., 2020. Complex interactions between large igneous province emplacement and global-temperature changes during the cenomanian-turonian Oceanic Anoxic Event (OAE 2). Paleoceanography Paleoclimatol. 35 e2020PA004016.
Peters, K.E., Peters, K.E., Walters, C.C., Moldowan, J., 2005. The Biomarker Guide. Cambridge university press.
Raiswell, R., Berner, R.A., 1987. Organic carbon losses during burial and thermal maturation of normal marine shales. Geology 15, 853–856.
Sanei, H., Grasby, S.E., Beauchamp, B., 2012. Latest Permian mercury anomalies. Geology 40, 63–66.
Sanei, H., Grasby, S.E., Beauchamp, B., 2015. Contaminants in Marine Sedimentary Deposits from coal Fly Ash during the latest Permian Extinction. In: Blais, J.M., Rosen, M.R., Smol, J.P. (Eds.), Environmental Contaminants: Using Natural Archives to Track Sources and Long-Term Trends of Pollution. Springer, Netherlands, Dordrecht, pp. 89–99.
Selby, D., Cumming, V.M., Rooney, A.D., Finlay, A.J., 2014. Hydrocarbons/Rhenium–Osmium (Re–Os): organic-rich sedimentary rocks. In: Rink, W.J., Thompson, J. (Eds.), Encyclopedia of Scientific Dating Methods. Springer, Netherlands, Dordrecht, pp. 1–7.
Shen, J., Yu, J., Chen, J., Algeo, T.J., Xu, G., Feng, Q., Shi, X., Planavsky, N.J., Shu, W., Xie, S., 2019. Mercury evidence of intense volcanic effects on land during the Permian-Triassic transition. Geology 47, 1117–1121.
Shen, J., Feng, Q., Algeo, T.J., Liu, J., Zhou, C., Wei, W., Liu, J., Them, T.R., Gill, B.C., Chen, J., 2020. Sedimentary host phases of mercury (Hg) and implications for use of Hg as a volcanic proxy. Earth Planet. Sci. Lett. 543, 116333.
Sial, A.N., Chen, J., Lacerda, L.D., Frei, R., Tewari, V.C., Pandit, M.K., Gaucher, C., Ferreira, V.P., Cirilli, S., Peralta, S., Korte, C., Barbosa, J.A., Pereira, N.S., 2016. Mercury enrichment and Hg isotopes in Cretaceous–Paleogene boundary successions: Links to volcanism and palaeoenvironmental impacts. Cretac. Res. 66, 60–81.
Smith, C.N., Kesler, S.E., Blum, J.D., Rytuba, J.J., 2008. Isotope geochemistry of mercury in source rocks, mineral deposits and spring deposits of the California Coast Ranges, USA. Earth Planet. Sci. Lett. 269, 399–407.
Sun, R., Enrico, M., Heimbürger, L.E., Scott, C., Sonke, J.E., 2013. A double-stage tube furnace–acid-trapping protocol for the pre-concentration of mercury from solid samples for isotopic analysis. Anal. Bioanal. Chem. 405, 6771–6781.
Svensen, H., Planke, S., Malthe-Sørenssen, A., Jamtveit, B., Myklebust, R., Rasmussen Eidem, T., Rey, S.S., 2004. Release of methane from a volcanic basin as a mechanism for initial Eocene global warming. Nature 429, 542.
Svensen, H., Planke, S., Polozov, A.G., Schmidbauer, N., Corfu, F., Podladchikov, Y.Y., Jamtveit, B., 2009. Siberian gas venting and the end-Permian environmental crisis. Earth Planet. Sci. Lett. 277, 490–500.
Sweeney, J.J., Burnham, A.K., 1990. Evaluation of a simple Model of Vitrinite Reflectance based on Chemical Kinetics1. AAPG Bull. 74, 1559–1570.
Tang, S., Zhou, Y., Yao, X., Feng, X., Li, Z., Wu, G., Guangyou, Z., 2019. The mercury isotope signatures of coalbed gas and oil-type gas: Implications for the origins of the gases. Appl. Geochem. 109, 104415.
Tang, Y., Jenden, P.D., Nigrini, A., Teerman, S.C., 1996. Modeling early methane Generation in coal. Energy Fuel 10, 659–671.
Them, T.R., Jagoe, C.H., Caruthers, A.H., Gill, B.C., Grasby, S.E., Gröcke, D.R., Yin, R., Owens, J.D., 2019. Terrestrial sources as the primary delivery mechanism of mercury to the oceans across the Toarcian Oceanic Anoxic Event (early Jurassic). Earth Planet. Sci. Lett. 507, 62–72.
Tissot, B.P., Welte, D.H., 1984. From Kerogen to Petroleum, Petroleum Formation and Occurrence. Springer, pp. 160–198.
Wang, J., Zhou, C., Xu, W., Liu, Z., Wang, S., Zhang, J., 2016. Shale gas exploration prospect evaluation in Lin'an block of the Northwest Zhejiang province. Geol. Surv. Res. 39 (2), 123–129 (in Chinese).
Wang, X., Cawood, P.A., Zhao, H., Zhao, L., Grasby, S.E., Chen, Z.-Q., Wignall, P.B., Lv, Z., Han, C., 2018. Mercury anomalies across the end Permian mass extinction in South China from shallow and deep water depositional environments. Earth Planet. Sci. Lett. 496, 159–167.
Wilhelm, S.M., National Risk Management Research Laboratory (U.S.), 2001. Mercury in Petroleum and Natural gas–Estimation of Emissions from Production, Processing, and Combustion. U.S. Environmental Protection Agency, National Risk Management Research Laboratory, Research Triangle Park, NC.
Yin, R., et al., 2016. Effects of mercury and thallium concentrations on high precision determination of mercury isotopic composition by Neptune Plus multiple collector inductively coupled plasma mass spectrometry. J. Anal. Atomic Spectro. 31 (10), 2060–2068.
Zhang, S., Wang, X., Wang, H., Bjerrum, C.J., Hammarlund, E.U., Costa, M.M., Connelly, J.N., Zhang, B., Su, J., Canfield, D.E., 2016. Sufficient oxygen for animal respiration 1,400 million years ago. Proc. Natl. Acad. Sci. 113, 1731–1736.
Zheng, W., Foucher, D., Hintelmann, H., 2007. Mercury isotope fractionation during volatilization of Hg(0) from solution into the gas phase. J. Anal. At. Spectrom. 22, 1097–1104.
Zheng, X., Dai, S., Nechaev, V., Sun, R., 2020. Environmental perturbations during the latest Permian: evidence from organic carbon and mercury isotopes of a coal-bearing section in Yunnan Province, southwestern China. Chem. Geol. 549, 119680.
Zhou, B.X., Sun, T., Shen, W., Shu, L., Niu, Y., 2006. Petrogenesis of Mesozoic granitoids and volcanic rocks in South China: a response to tectonic evolution. In: Episodes, 29, p. 26.